Water-mediated synthesis of halide solid electrolyte and conducting polymer hybrid materials for all-solid-state batteries

Elina Nazmutdinova [b,c,d] Carolin Rosenbach[e] Christina Schmidt[a] Sangchai Sarawutanukul[f] Kerstin Neuhaus[a] André Gröschel[b,c,d] and Nella M. Vargas-Barbosa[a,d]*

[a]Forschungszentrum Jülich GmbH, IEK-12: Helmholtz Institute Münster, Corrensstrasse 46, 48149 Münster, Germany

[b]Institute of Physical Chemistry, University of Münster, Corrensstrasse 28/30, 48149 Münster, Germany

[c]Center for Soft Nanoscience, University of Münster, Busso-Peus-Str.10, 48149 Münster, Germany

[d]International Graduate School for Battery Chemistry, Characterization, Analysis, Recycling and Application (BACCARA), University of Münster, Corrensstrasse 40, 48149 Münster, Germany

[e]Institute of Inorganic and Analytical Chemistry, University of Münster, Corrensstrasse 28/30, 48149 Münster, Germany

[f]Centre of Excellence for Energy Storage Technology (CEST), Department of Chemical and Biomolecular Engineering, School of Energy Science and Engineering, Vidyasirimedhi Institute of Science and Technology (VISTEC), Rayong 21210, Thailand

*corresponding author (n.vargas-barbosa@fz-juelich.de)

Abstract:

Over the last decades, we have seen an increase in the number of new materials that can be incorporated into all-solid-state batteries (ASSBs). Halide solid electrolytes have attracted significant attention due to their superior stability against oxide-based cathode active materials when compared to sulfide-based solid electrolytes. Nonetheless, the dynamicity of interparticle contact during cycling in ASSBs hinders their stability and performance. Therefore, inactive materials such as electronically conductive additives and polymer binders are needed to compensate the contact-loss reducing the energy density of the resulting cells. Here, we present an aqueous approach for the preparation of halide solid electrolyte-conductive polymer hybrid composites with Li_3InCl_6 and poly(3,4-ethylendioxythiophene)/poly(styrene sulfonate) (PEDOT:PSS) in one-pot. The resulting

composites combine the properties of a solid electrolyte with a conductive additive and a binder together with into a single hybrid material. Together with other analytical techniques, Kelvin Probe Force Microscopy (KPFM) imaging showed a successful synthesis of the hybrid materials and revealed that the conductive polymer (CP), namely PEDOT:PSS, is located at the surface/grain of the Li_3InCl_6. Upon incorporation of such composites in sulfide solid-state half-cells with lithium nickel manganese cobalt oxide (NMC) cathode active material (CAM) we observe an increase in the partial electronic transport of the catholytes with increasing CP content, which correlates an increase in the initial discharge capacities. This study sets the stage to explore the preparation of multi-functional catholytes without the necessity of organic solvents, extremely high temperatures or special environments.

Introduction

Worldwide decarbonization goals made the electrochemistry research field take a center stage both at the industrial and academic scenes. With already matured liquid-electrolyte-based Li-ion-battery technology, numerous scientists address the safety and performance issues through the development of ASSB solutions.[1] Hence, ASSBs are seen as promising candidates to surpass conventional lithium-ion batteries because they offer advantages in numerous aspects, including both electrochemical and safety performance for various cell-chemistries.[2–4] Additionally, the use of solid electrolytes (SE) enabled the possibility to replace graphite anodes with high-energy-density lithium metal.[5,6] This opened the paths to a new generation of lithium metal solid-state batteries (LMSSBs).

Notwithstanding diverse advantages, various challenges that still hamper the performance of LMSSBs must be addressed by the scientific community. The electro-mechano-chemical degradation of ASSB cathodes is one of them.[7,8] The expansion/contraction of the CAM leads to the loss of the interparticle contact between the CAM and SE. This makes a targeted design of the CAM-SE interface of high importance.[9,10] Polymer binders are frequently used to mitigate interparticle contact loss and provide additional mechanical stability in battery electrodes.[11,12] Polymers are however often intrinsic insulators and cannot provide electronic conductivity throughout the cathode active components. This necessitates the addition of conductive additives (e.g. conductive carbon) which at the same time increases the overall volume of non-active components in the cathode composite.[13,14] Thus, a cathode composite, a so-called catholyte, consists of CAM, SE, and functional additives.

To tackle the described problems, we propose the use of a functional binder within the cathode composite. Electronically conducting polymers, instead of conventional carbon additives, can help improve interparticle contact, both physical and electronic. Specifically, we can increase the partial electronic conductivity in the cathode composites, which in turn increases the amount of addressed active material without a significant increase in the volume of non-active components. This is expected to boost the transport of electrons during cycling along with an improved initial capacity of the cell.

As a candidate for an electronically conductive binder, derivatives of 3,4-ethylendioxythiophene (EDOT) were surveyed. Known for their outstanding electrical and good mechanical properties, polymerized EDOT, i.e. poly(3,4-ethylendioxythiophene) (PEDOT) found numerous applications in energy conversion and storage devices.[15] Consequently, the use of EDOT-based polymers was reported to improve the performance of lithium-ion batteries with liquid-electrolyte (when used as a cathode binder) and in high-performance silicone batteries (when used as an anode-binder).[16–20] Additionally, the use of the PEDOT in the mixture with SE was shown to improve charge transfer kinetics within the lithium cobalt oxide-based catholyte proved by density functional theory calculations.[21]

Poly(3,4-ethylendioxythiophene)/poly(styrene sulfonate) (PEDOT:PSS) has become the polymer of our choice (see Figure S1 for the chemical structure). Showing moderate intrinsic electronic conductivity and being commercially available, PEDOT:PSS can be redispersed in water due to the presence of hydrophilic -SO_3H groups in PSS. Thus, we decided to benefit from the advantageous properties of PEDOT:PSS and use it as a component in the catholyte composite for ASSBs. A direct substitution of the inactive binder and the conductive additive with a single polymer material is expected to result in catholytes that can accommodate volume changes during cycling and provide sufficient electronic conductivity. PEDOT:PSS therefore possesses a dual functionality in our catholyte for ASSB: providing the additional electronic pathways and acting as a binder for the CAM and SE.

To design a catholyte system, we considered numerous aspects, including both the electrochemical stability of the components and their facile processability. The sulfides, a class of SE with the highest reported ionic conductivity (>10 mS/cm), suffer from degradation against high voltage transition metal oxide CAM due to their narrow electrochemical stability window.[22–24] The latter limits the overall performance of the SSB cell as the most-performant cathodes are difficult to be used. Conversely, oxides are stable but require high-energy processing.[22,25] That is why the recently developing class of SEs, superionic halides, has received much attention.[26] Not only do they show high electrochemical stability towards high-

potential cathode active materials, but they can be synthesized *via* water-mediated synthesis.[26–29] To develop a novel catholyte composite we were inspired by the water-mediated *in-situ* interfacial growth of lithium indium chloride, i.e., Li_3InCl_6, on the CAM, when the SE grows onto the particles of the cathode material.[30] But as numerous issues were reported that arise from the perturbed electron transport for coated CAM particles,[31] we decided to revisit the approach. [31]

Here, we demonstrate a water-based synthesis of a composite containing an electronically conductive binder and Li_3InCl_6 by *in-situ* crystallization of Li_3InCl_6 in the matrix of redispersed bifunctional CP. The developed synthesis route provided high-purity Li_3InCl_6 particles covered with CP binder as demonstrated by scanning electron microscopy (SEM), energy dispersive X-ray (EDX) spectroscopy, and KPFM measurements. This composite was mixed with an NMC-based CAM and the electrochemical performance of the cathode composites was evaluated *via* partial electron conductivity measurements and cycling in sulfide SSB half-cells. We observe an increase in the initial discharge capacities of the cells with increasing polymer content in the hybrid materials. Although there is significant room for further optimization, our results set the stage for the processing of catholyte components in a reduced number of steps (one-pot and using green solvents (water), without compromising the expected performance of the cells.

Experimental section

Materials. Lithium chloride (LiCl, Alfa Aesar, 99 %), indium chloride ($InCl_3$, Alfa Aesar, 99,99 %), PEDOT:PSS (Sigma Aldrich, redispersible pellets, CP), NMC622 ($LiNi_{0.6}Mn_{0.2}Co_{0.2}O_2$, MSE Supplies, NMC622), lithium phosphorus sulfur chloride, i.e., sulfide argyrodite (Li_6PS_5Cl, MSE Supplies, 325 mesh), lithium (Li, 99.9%), indium (In, chemPUR, foil, 100 μm thickness, 99.999 %).

Synthesis of Li_3InCl_6. The halide solid electrolyte, Li_3InCl_6, was synthesized *via* a water-mediated process adapted from previously reported procedures.[29,32,33] Dried components, LiCl and $InCl_3$ were weighed out and mixed in an Ar-filled glovebox ($p(O_2) < 0.1$ ppm, $p(H_2O) < 0.8$ ppm) in a 3:1 stoichiometric molar ratio. The mixture of the precursors was dissolved in distilled water (up to 5 mL) in a vial outside of the Ar-filled glovebox. Upon full dissolution of the reagents, water was evaporated at 60 °C for 8 h. A magnetic stirrer was used during the evaporation step for 4 h until Li_3InCl_6 crystallization was observed. The hydrated form of

Li_3InCl_6 ($Li_3InCl_6 \cdot xH_2O$) was subjected to vacuum drying at 200 °C for an additional 8 h to remove the residual water. The as-synthesized Li_3InCl_6 (white powder) was transferred into the Ar-filled glovebox and hand-ground for 15 min in an agate mortar before further use.

Synthesis of Li_3InCl_6|CP composites. Dry LiCl and $InCl_3$ were weighed in a 3:1 molar ratio, along with different amounts of dried PEDOT:PSS in an Ar-filled glovebox. The weighed amount of CP was chosen to correspond to a final 1, 2, or 5 wt% of CP with respect to the expected Li_3InCl_6. The mixture of Li_3InCl_6 precursors as well as the CP were dissolved in distilled water in separate vials and mixed until fully dissolved. Upon dissolution of the components, the aqueous solution of Li_3InCl_6 precursors was transferred into the vial of the redispersed CP and thoroughly mixed. Subsequently, water was removed at 80 °C for 12 h without additional mixing during water evaporation. The composite was obtained in a form of dry light gray powder and transferred to a vacuum oven at 200 °C for two dehydration steps (each 4 h). The synthesized composite was hand-ground for 15 min in the agate mortar in between and after the vacuum drying steps inside the Ar-filled glovebox. The obtained product, namely Li_3InCl_6|CPX with X = 1, 2, 5 % corresponding to wt% of added CP, was used for characterization and as component of the catholyte in sulfide half-cells.

Preparation of the catholytes. For preparing 4 different catholytes, the NMC622 CAM was introduced separately into Li_3InCl_6, Li_3InCl_6|CP1%, Li_3InCl_6|CP2%, and Li_3InCl_6|CP5% at a ratio of 70:30 wt% and hand ground for 30 min in an agate mortar. Thus, the following cathode composite types were obtained: NMC622|Li_3InCl_6 and NMC622|Li_3InCl_6|CPX (with X = 1, 2, 5 %).

Powder X-ray Diffraction (PXRD). The phase purity of the Li_3InCl_6 in SE and hybrid samples was evaluated by PXRD in a Stoe STADI P diffractometer (Debye-Scherrer geometry, Dectris MYTHEN 1K detector). Cu K_α radiation (λ = 1.54 Å) with Ge 111 monochromator was used to acquire spectra within a 2θ range of 10 – 70 °. The powder samples were measured in airtight glass capillaries sealed with grease. The scans were recorded with steps of 3 ° and a step time of 120 s.

Thermal analysis. TGA Q5000IR (TA Instruments) was used to carry out the thermogravimetric analysis (TGA). A standard procedure applied heating the samples

(Li_3InCl_6, CP, and Li_3InCl_6|CPX) with a rate of 10 °C/min in the range of 30 °C – 900 °C in an alumina pan, supported by a high temperature platinum pan under nitrogen gas flow of 25 mL/min. It should be noted that the samples were exposed to air for a short time when the samples were transferred into the open alumina crucibles straight from the Ar-filled air-tight transfer module until the samples were placed in the system of the TGA instrument under nitrogen gas flow. To minimize the exposure to the humidity from air, the Al pans of selected samples were crimped inside of the glovebox. Subsequently, the air-tight pans were pinned with a needle directly before the TGA measurement performed in the temperature range of 30 °C – 600 °C under nitrogen gas flow (25 mL/min). For analyzing the stability of as-received CP in the presence of oxygen, a TGA measurement was performed in the temperature range of 30 °C – 1000 °C under oxygen gas flow (25 mL/min). The treatment of the TGA results was complemented by derivative thermogravimetry (DTG) which shows the derived weight changes upon heating plotted against temperature.
Differential scanning calorimetry (DSC) measurements were performed in aluminum pans (sealed hermetically in dry room conditions) using a DSC Q2000 (TA Instruments) with a heating rate of 10 °C/min in a temperature range between 0 °C – 250 °C. The samples were subjected to 3 temperature regimes: heating/cooling cycle followed by the second heating.

SEM and EDX. SEM equipped with an Auriga CrossBeam working station from Carl-Zeiss with a field emission gun (Schottky-type) under an acceleration voltage of 3 kV was used to investigate the morphology of the synthesized Li_3InCl_6 and hybrid composites as powders and in pelletized form. Imaging was performed with an InLens secondary electron detector. The powder samples were dispersed and pressed pellets were placed onto carbon tape attached to SEM stubs and further sputtered with Pt (sputtering layer thickness 10 nm) inside the Ar-filled glovebox. Transfer of the samples from the glovebox was handled in an in-house-designed SEM vacuum sample holder minimizing exposure to air. To study the elemental composition of the samples, EDX with X-Max 80 mm^2 detector under 15 kV of acceleration voltage was used. The acquired data was evaluated with the INCA software (version 5.05, Oxford Instruments).

Raman Spectroscopy. Sample preparation for Raman characterization included placing each sample on a microscopy glass slide and sealing it with Kapton® tape inside the glovebox. A Bruker Senterra Raman microscope (laser: 532 nm, 2.5 mW) was used for the measurements. The spectra (resolution 3–5 cm^{-1}) were acquired in the range of 100 – 1700 cm^{-1} of Raman

shift. Coaddition and integration time varied to obtain resolvable spectra: from 5 – 10 s for integration time and 10 – 15 coadditions. The obtained results were treated using the OPUS 7.5 software.

KPFM. KPFM measurements were performed with a Cypher ES AFM system (Oxford Instruments) using ASYELEC-01-R2 tips with a Ti/Ir coating. These tips enable measuring topography parameters and the local surface potential (contact potential difference between Ti/Ir and sample) with a high lateral resolution. The samples were measured in Ar at a constant sample temperature of 32 °C. Measurements were performed in a dual-pass mode: in the first step, the sample topography and changes in the amplitude and phase of the AFM cantilever (which is vibrating at its resonance frequency in free air) are recorded. In the second step, the tip is moved to a certain height above the surface and the surface potential (also known as the Volta potential) is measured.[34] In addition, information about the local elasticity and adhesion forces can be derived from the variation of the phase signal of the cantilever vibration in interaction with the sample surface. An increase in elasticity and/or local adhesion forces lead to an increased phase signal in this region.

Electrochemical characterization. All measurements were performed in press cells based on a previously reported design that includes a PEEK-based cylindric inlet (10 mm diameter) confined between two stainless-steel current collectors.[35] The assembly of the cells was done inside an Ar-filled glovebox.

Ionic conductivities of as-synthesized Li_3InCl_6 were determined with alternating current (AC) impedance spectroscopy on a VMP-300 potentiostat (BioLogic) in the temperature range of 233 – 333 K (-40 – 60 °C). The press cells were filled with 250 mg of Li_3InCl_6. The samples were scanned in the frequency range of 100 mHz – 7 MHz with 10 mV of applied sinus amplitude at open circuit potential. The analysis of the recorded spectra was performed in RelaxIS 3 software (rhd Instruments).

Partial electronic conductivities of the cathode components and the composites were determined *via* direct current (DC) polarization measurements in symmetric cells with ion-blocking, i.e., stainless steel electrodes. A set of different potentials (5 mV, -10 mV, 20 mV, 30 mV) were applied to the symmetric cells at 25 °C. The sample mass was ca. 50 mg.

For both the ionic conductivity and partial electronic conductivity measurements, the sample was loaded in the polyether ether ketone (PEEK) inlet of the press cell and subsequently uniaxially pressed with an applied pressure of 3 t for 3 min with a slow pressure release.

The sulfide half-cells for galvanostatic charge-discharge studies were assembled in multiple steps. In the first step, 60 mg of Li_6PS_5Cl and 50 mg of pristine Li_3InCl_6 were pressed as a bilayer pellet at 2 t for 1 min. Then, 12 mg of the cathode composite (preparation described in section 2.1.3) was loaded on top of the Li_3InCl_6-side of the bilayer SE pellet, evenly spread, and pressed at 3 t for 5 min. This amount of cathode composite corresponds to 10.7 mg/cm^2 aerial loading and an aerial theoretical capacity of 2.14 mAh/cm^2 (based on a theoretical specific capacity of NMC622 of 200 mAh/g). Subsequently, the anode side of the cell was prepared by punching out foils from hand-pressed Li (obtained film of 200 μm thickness, 6 mm diameter) and commercial In foil (9 mm diameter). The metal foils were stacked together to form a stable alloy and placed with In metal adjacent to the argyrodite side of the bilayer SE separator and with Li to the stainless steel electrode.[36] Finally, the cell was placed in a homemade stainless-steel holder with an applied pressure of ca. 125 MPa. The cells were cycled at 0.1 C (applied current density of 0.214 mA/cm^2) in the potential range of 2.6 – 4.3 V *vs*. Li/Li$^+$, considering that 0 V vs. In/LiIn = 0.62 V *vs.* Li/Li$^+$.[36]

Results and Discussion

As a first step, we reproduced the previously reported water-mediated synthesis of Li_3InCl_6.[29,32,33] Figure 1a shows the PXRD spectra of Li_3InCl_6, where all reflections align well with the reference pattern for the compound. As a comparison, we also considered the reference pattern for indium oxychloride (InOCl), a common side-product in the preparation of Li_3InCl_6, and no reflections match this side phase.[14,29,33,37] Similar to previous reports on the synthesis of Li_3InCl_6, we also observe two reflections (at 17.25 ° and 19 °) which we cannot assign to a specific phase but it is presumably a side-phase in low yields that does not affect the ionic conductivity of the material (see discussion below).[14,28,29,33,37,38]

Temperature-dependent impedance spectra (Figure S2) were analyzed to determine the ionic conductivity of the Li_3InCl_6 (Figure 1b). We obtain a room temperature total ionic conductivity of 1.36 mS/cm and an activation barrier of 0.42 eV, both values within the range of those reported by other groups.[28,29,32,37] A representative SEM image of the as-synthesized Li_3InCl_6 powder is shown in Figure 1c. The synthesis produces coarse, elongated particles within the

10-60 µm size range. The EDX elemental mappings of a single Li_3InCl_6 particle (Figure 1d) show uniform distribution of In and Chlorine (Cl) (Figure 1e, f). Despite careful handling of the samples inside an Ar atmosphere, oxygen signals (< 3 wt%) were identified for the SE (Figure S3). The detected oxygen can be attributed to the air leakages inside the transfer module when the samples were transferred from the synthesis glovebox into the glovebox for sputtering, the non-ideal tightness of the home-made SEM-vacuum sample holder, and the presence of water-residues after water-mediated synthesis. The latter can be excluded upon thorough investigation of the thermal properties of the compound.

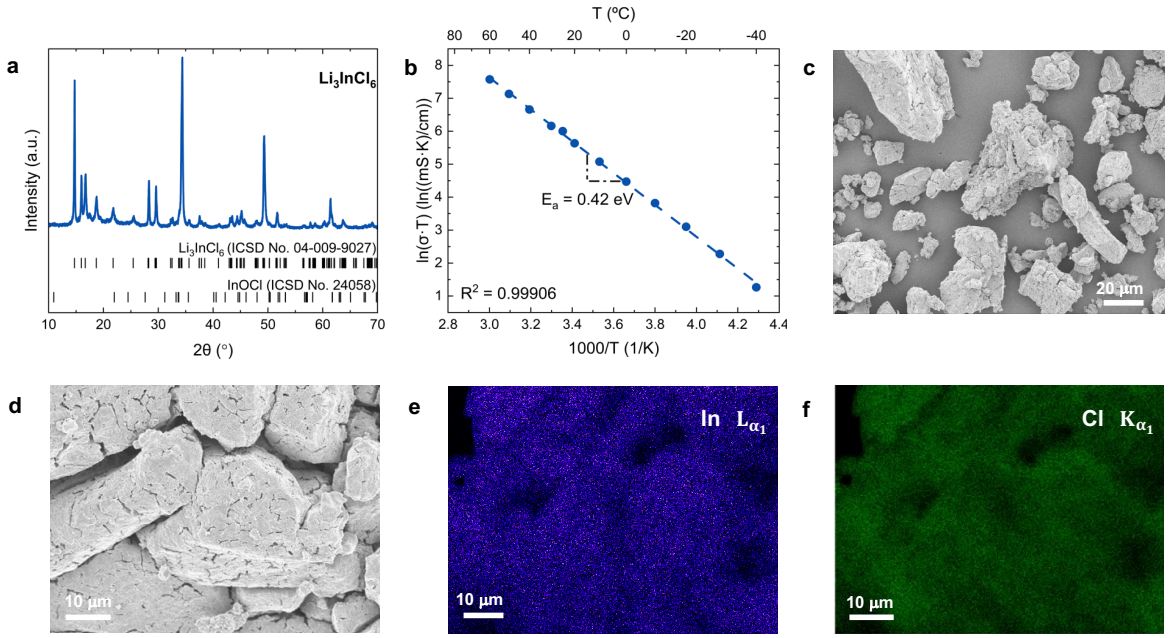

Figure 1. *Crystal structure and electron microscopy characterization of as-synthesized Li_3InCl_6. (a) PXRD pattern, including reference indices for the target compound and InOCl side-phase, (b) Arrhenius plot of Li_3InCl_6, (c and d) SEMs of the Li_3InCl_6 powder, (e and f) EDX analysis for In and Cl from the image in (d).*

TGA and DTG analysis of the samples analyzed in open alumina crucibles showed that Li_3InCl_6 undergoes several processes within the 0 – 900 °C temperature window (Figure S4a). Firstly, a 2.1 wt% loss at 90 – 150 °C can be assigned to the water evaporation from the particle surface. A second transition amounting to 60 wt% weight loss is observed in the range of 350 – 570 °C and is assigned to the melting of the Li_3InCl_6, as previously reported.[39] The final decomposition of the SE occurs at temperatures above 760 °C. To ascertain that the initial transition corresponds solely to adsorbed water, we took further precautions in the sample preparation and measurement process to minimize sample exposure to wet air. In doing so, we

were able to reduce the water content in the Li_3InCl_6 sample to 0.35 wt% (Figure S4b). The calorimetry results based on DSC measurements show no sign of adsorbed water in the sample (Figure S4c). Note however that for DSC measurements the samples were never exposed to air, neither during sample preparation nor during the measurement itself. The latter results demonstrate that the as-synthesized Li_3InCl_6 is dry and can be used when handled in inert gas atmospheres. Taken together, the TGA and DSC results show that the Li_3InCl_6 is thermally stable during the synthesis with the water evaporation step (80 °C in air), as well as during the vacuum drying of the Li_3InCl_6 (200 °C), and also show that the remaining water should evaporate completely in the second step at 200 °C.

TGA of the as-received, water-redispersible electroconductive polymer, PEDOT:PSS, shows that the polymer is stable in oxygen and in inert atmosphere in a wide temperature window (Figure S5a-b). Since the decomposition of the CP in O_2 starts at 250 °C, it can be safely used as a component for the composite synthesis performed in the temperature range of 25 °C – 200 °C. The DSC results (Figure S5c) suggest that CP does not undergo any phase transformations in the investigated temperature range. The endothermic peak at 150 – 180 °C can be attributed to the energy release from water evaporation. The peak fully disappears during the second heating cycle meaning that the sample no longer contains residual water. The composite samples were prepared with the use of the fully dried CP weighed out in the glovebox environment.

A schematic description of the one-pot composite preparation approach is presented in Figure S6. The specific synthesis conditions were obtained *via* trial-and-error optimization of various parameters, such as temperature of water evaporation, annealing temperatures, and precursor mixing conditions. Figure S7 compares the PXRD patterns of Li_3InCl_6|CP5% samples prepared with unoptimized conditions to those further used in this study. For the unoptimized sample, we can clearly distinguish the residual presence of precursors as well as multiple side-phases.

The presence and stability of the CP in the composites prepared with optimized conditions was evaluated with various complimentary methods. Raman spectra show that addition of the polymer leads to the appearance of the peaks that can be attributed exclusively to the PEDOT and PSS moieties and can be distinguished despite the broad background caused by Li_3InCl_6 in the range of 900 – 1600 cm^{-1} (Figure 2a, blue trace). Li_3InCl_6 has various characteristic bands in the range of 100 – 300 cm^{-1}, and a particularly strong one at ca. 290 cm^{-1}. Indeed, the latter band is easily distinguished in both the pure Li_3InCl_6 as well as all the composite samples.[40,41]

Similarly, the most distinguishable Raman fingerprints of the PEDOT in the composite are the bands appearing at 440, 578, and 988 cm^{-1}, characteristic for oxyethylene ring deformation, as well as the band at 1445 cm^{-1}, assigned to the symmetric stretching of carbon-carbon double bond.[42–44] The signal expected from vibrational modes from PSS moiety is the peak appearing at 1100 cm^{-1}, which is clearly distinguishable for all composite samples.[44–47] Figure 2b shows the PXRD patterns that confirm a high purity of Li_3InCl_6 in the composites at all CP wt%. Small reflections at 13 ° and 31 ° were detected for the sample of Li_3InCl_6|CP5% that are often found in halide compounds and can be assigned to the presence of the hydrated Li_3InCl_6 in very small amounts.[32,38,48]

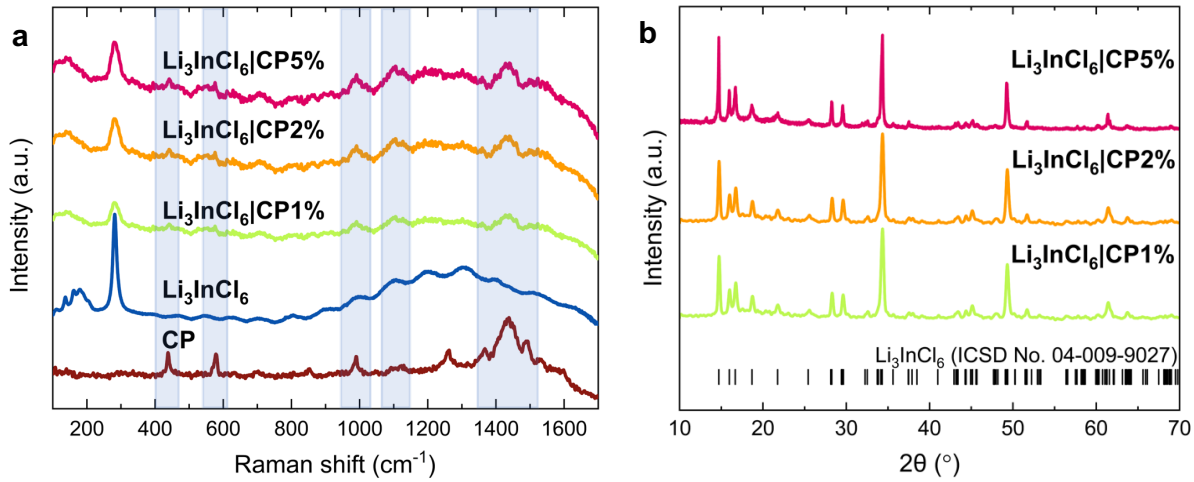

Figure 2. *(a) Raman spectra of the Li_3InCl_6|CPX composites at various wt% of the CP, as-synthesized Li_3InCl_6 and CP. The shaded regions highlighted in (a) are characteristic bands for the CP component. (b) PXRD patterns of the Li_3InCl_6|CPX composites, including reference indices for the target main-Li_3InCl_6 phase.*

The TGA of the composites was also performed in open alumina crucibles for samples with different CP loadings (Figure S8). In general, all composites show an initial weight loss of ca. 2 – 3 wt% at 90 – 150 °C, which is assigned to water evaporation. Similar to the Li_3InCl_6, the composites degrade in 2 steps: ca. 60 wt% loss at 350 – 570 °C followed by the final decomposition at temperatures over 650 °C. Figure 3a shows exemplary results for the Li_3InCl_6|CP5% sample characterized using the modified sample preparation procedure to minimize exposure to ambient air. For such samples, only a mass change of 0.08 wt% attributable to water evaporation in the range of 110 – 150 °C was observed. Results of the

DSC for composites with different CP loadings (Figure S9 and Figure 3b) exclude any phase transitions in the temperature range used for the synthesis of the composites.

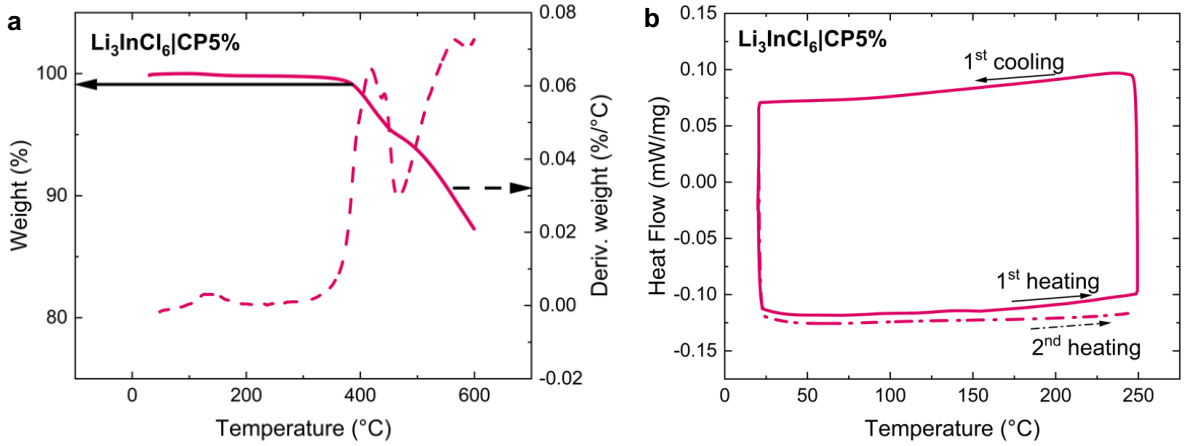

Figure 3. *(a) TGA (solid) and DTG (dashed) of the Li_3InCl_6|CP5% composite under nitrogen flow performed in a tightly sealed aluminum crucible crimped inside the glovebox pinned shortly before the measurement, (b) DSC of the Li_3InCl_6|CP5% composite from two heating and one cooling cycle.*

SEM images show that the Li_3InCl_6 particles in the composites retain sizes comparable to the pristine as-synthesized Li_3InCl_6 (Figure 4a-b), while EDX mappings shows a homogenous distribution of In, Cl, sulfur (S) (Figure 4c-e and Figure S10). This suggests that the CP (which contains both sulfur and oxygen) is homogenously distributed in the composite samples. The SEM-EDX results for Li_3InCl_6|CP1% and Li_3InCl_6|CP2% show similar elemental distributions (Figure S11 – S12).

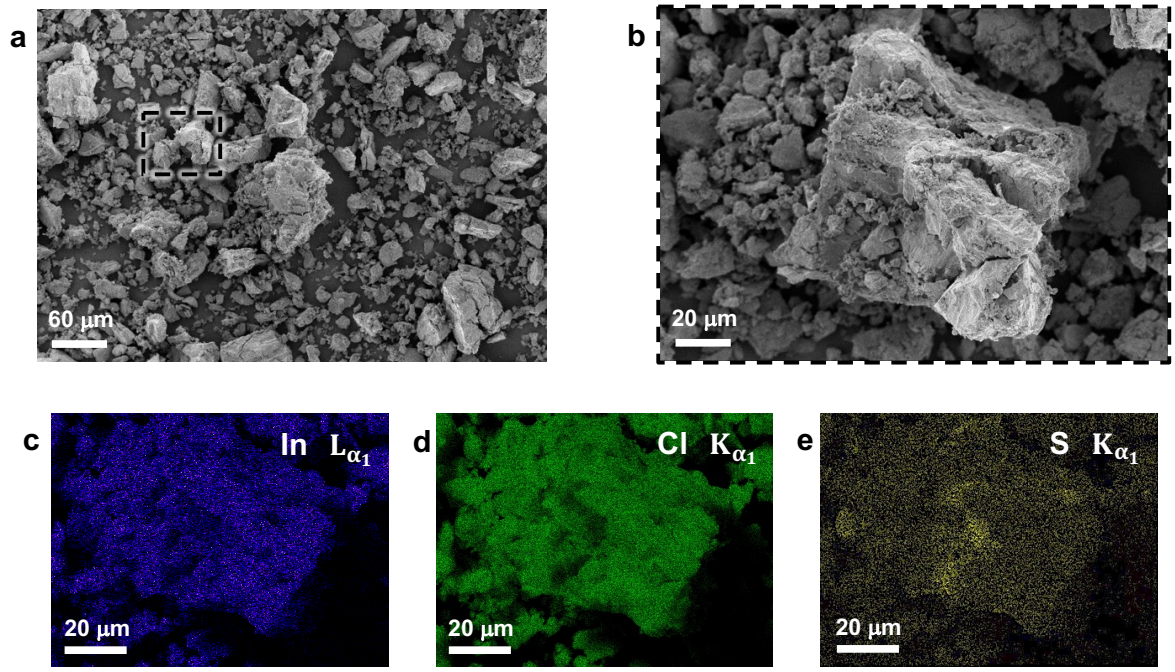

Figure 4. *(a and b) SEMs of the Li_3InCl_6|CP5% powder, (c - e) EDX analysis for In, Cl and S from the image in (b).*

A more direct method to probe the distribution of the CP in the composite samples is KPFM. The latter is an extended atomic force microscopy (AFM) method that can directly measure both the topography and surface potential of a flat sample. Such samples were prepared by pressing the SE and hybrid powders at 374 MPa for 3 min. Figure S13 and Figure S14 show the SEM and EDX characterization of such pressed powders was done to confirm the integrity of the samples upon processing prior to further analysis.

For a surface potential measurement by KPFM, an AC potential with a frequency close to the mechanical resonance frequency and a given amplitude was applied to the AFM tip. This AC potential is fixed by an additional external voltage U_{DC} which compensates the surface potential difference between sample and probe tip according to:

$$U_{KPFM}=-\frac{1}{e}\Delta\varphi_{CPD}=U_{DC}$$

A plot of the potential difference U_{DC} during the surface scan of the AFM tip yields the KPFM map.[49,50] The value in the KPFM images is the contact potential difference ($\Delta\varphi_{CPD}$) between the AFM tip coated with titanium/iridium (Ti/Ir) and the sample. The working hypothesis here is that the absolute value of the contact potential difference ($|\Delta\varphi_{CPD}|$) between the electronically conductive polymer and the Ti/Ir tip should be smaller than that of the contact potential difference between the SE particles and the tip. As the measured potentials are all negative,

areas which are covered in a thicker layer of polymer should show up as lighter areas in the image.

In Figure 5 we compare the topography and surface potential images for a pristine Li_3InCl_6 and the Li_3InCl_6|CP5% composite samples. We notice that at this length scale the particle (grain) size of the Li_3InCl_6 differs such that the Li_3InCl_6 in the composites is smaller than in the pristine Li_3InCl_6 sample. In fact, although the particle size distribution is heterogeneous for both samples, the average grain size for pristine Li_3InCl_6 is the order of hundreds of nm (Figure 5a), whereas the grains in the composite range from tens to hundreds of nm (Figure 5c). In the case of the surface potential images we see more drastic differences between the two samples. The image for the pristine sample is in most cases heavily blurred and stripy (Figure 5b), which normally is a sign for electrostatic charging effects often observed for samples with low electronic conductivities. Since Li_3InCl_6 is a SE with reported electronic conductivities in the range of 10^{-9} – 10^{-10} S/m, this is an expected result.[28,29] We confirmed such poor electronic conductivities for the as-synthesized Li_3InCl_6, and we calculated a value of $2.08 \cdot 10^{-9}$ S/m from DC polarization measurements shown in Figure S15. For the Li_3InCl_6|CP5% composite sample we can identify increased (less negative) surface potentials at the edges and in the boundaries between adjacent grains. Since the net variation in surface potential for our composite samples is small (< 50 mV), e.g. the difference between the grain boundaries and grain interior of undoped garnet-type lithium lanthanum zirconate ($Li_7La_3Zr_2O_{12}$, LLZO) is in the range of 400 mV, it is important to consider the topography and phase angle images to make correct assignments in the surface potential.[51] In Figure 5e we observe specific regions (marked with arrows) where the grain boundaries show a higher phase contrast (lighter coloring) than the grains, which is generally associated with an increased elasticity and/or adhesion compared to the surrounding. In this region, we also observe minor topography changes (only a few nm, Figure 5d) and the surface potential shows some measurable differences/structure (Figure 5e). A direct comparison of the surface potential images shows that the pristine Li_3InCl_6 sample has an overall lower (more negative) potential than the Li_3InCl_6|CP5% composite, which serves as definite evidence of the incorporation of the conductive polymer and its effect on its electrical properties. The fact that differences in the phase image of the composite sample (Figure 5e) are in a similar range to the pristine LIC sample also indicates that the addition of the conductive polymer binder does not significantly change the (local) elasticity of the composite sample for the analyzed Li_3InCl_6|CP5%. Note that greater surface potential differences are also observed in other regions of the probed area (marked with circles). However, the circled area also corresponds to grain edges with large topographical differences and are therefore

interpreted as artefacts. Despite this, it is reasonable to interpret these results such that that the CP is located at the surface/grain boundaries between Li_3InCl_6 particles in the composite sample.

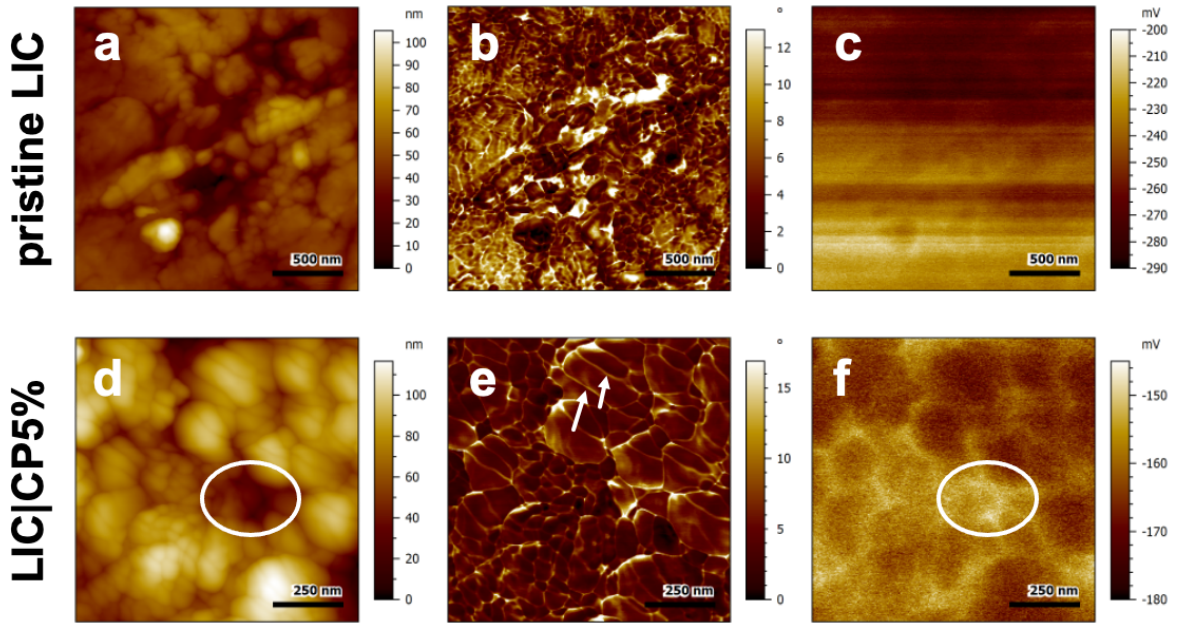

Figure 5. *Exemplary topography (a and d), phase (b and e) and surface potential (c and f) images for the pristine Li_3InCl_6 sample (upper row) and the Li_3InCl_6|CP5% composite samples (bottom row).*

Taken together, the TG, Raman spectroscopy, diffraction, and microscopy results (both SEM and KPFM) suggest that we have successfully synthesized SE|CP composites using a one-pot water-mediated synthesis route, in which the polymer is well-distributed in the halide SE.

The final step was to evaluate the (bulk) electrochemical properties of such composites when used as a catholyte component for NMC-based solid-state cells. Firstly, we determined the partial electronic conductivity of the samples *via* DC polarization (Figure 6a). To do this, the Li_3InCl_6|CPX composites were mixed with NMC622 (30:70 wt%) and subsequently pressed as pellets. SEM and EDX results suggest that both the Li_3InCl_6|CP5% composite and the NMC622 remain unharmed during processing (Figure S16). We observe that the partial electronic conductivity of the cathode composite increases four-fold upon the incorporation of 1 wt% of CP in the cathode composite in comparison to just Li_3InCl_6 combined directly with NMC622. Moreover, upon further increasing the CP content, we measure a monotonic increase in the partial electronic conductivity of the cathode composites.

Such cathode composites were then integrated into solid-state (half-)cells. Due to the well-known instability of the halide SE against Li metal, we tested these cathode composites in cells that used a bilayer separator with Li_6PS_5Cl and Li_3InCl_6 layers against In/LiIn as an anode.[52,53] Moreover, in this configuration we can truly focus on the effect of the cathode additives, namely the Li_3InCl_6|CP composites, on the performance of the cells. Figure 6b shows exemplary charge-discharge curves for the NMC622|Li_3InCl_6 catholyte, with an initial discharge capacity of 120 mAh/g that decays over the course of 30 cycles to ca. 100 mAh/g. The cathode composite with the highest CP content in this study (5 wt%) shows initial discharge capacities of almost 160 mAh/g and decays to 140 mAh/g over the course of 30 cycles (Figure 6c). The charge-discharge curves for the other two composites are compiled in Figures S16. Furthermore, the Coulombic efficiencies of all cells are summarized in Figure S18. In Figure 6d we compare the average performance of all cells tested and can confirm a monotonic increase in the initial discharge capacity of the cells with increasing CP content. Interestingly, the cycling stability of the cells does not correlate with the amount of CP in the cathode composite. The cells with better capacity retention are those with 2 wt% of CP, in which a capacity fade of only 4 % is observed over the course of 30 cycles, similarly showing highest Coulombic efficiency amounting to 99.6 %.

Although a direct comparison with the results reported by other research groups is challenging due to the different cell chemistries and active material loadings, our cycling results are comparable to previous reports in terms of delivered capacities.[26,37] As such, further optimization with respect to the relative ratios of all cathode components can result in improved initial and long-term performance of the cells. It was recently reported that cathode composites in which the partial ionic and partial electronic conductivities are matched, maximize the specific capacities of sulfide half-cells.[54,55] Such systematic optimization efforts are currently underway in our group. Moreover, previous reports have shown that the processing of solid-state materials, e.g., ball-milling versus hand-grinding, can have a strong impact in their electrochemical properties and solid-state battery performance.[56] Therefore, the processing approach for the preparation of the cathode composites is another parameter space that can be explored and may result in better performing cells. Ideally though, we can extend our optimized one-pot, water-mediated synthesis to incorporate cathode active materials directly and prepare the catholyte powder in a single, scalable step.[30]

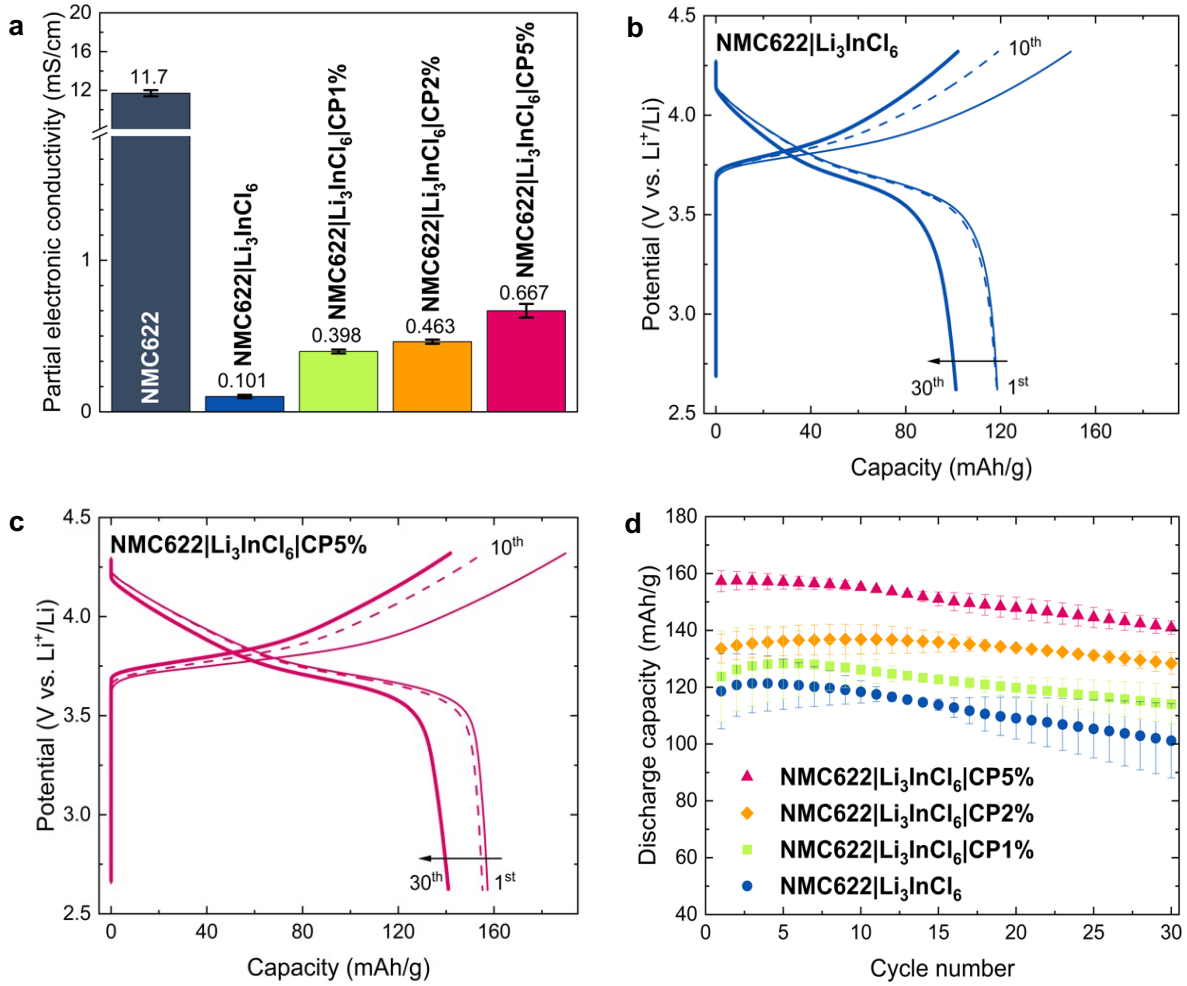

Figure 6. *Evaluation of electrochemical performance of the composites. (a) Partial electronic conductivities measured via DC polarization, (b and c) charge-discharge curves of the cells (b) without and (c) with CP (5 wt% to Li_3InCl_6) in the catholyte composite, (d) discharge capacities up to 30 cycles for cells with different catholyte composites at 0.1 C.*

4. Conclusions

In summary, we report a one-pot water-mediated synthesis of halide solid electrolyte-conductive polymer composites. The synthesis conditions have been optimized such that high purity Li_3InCl_6 is embedded in a well-distributed matrix of PEDOT:PSS, acting both as a binder and electronically conducting additive. The latter claim is supported by the following techniques: PXRD, TA, SEM, Raman, and KPFM. It was shown that the composites remain unharmed even after mixing with NMC622 and pressing in pellets. DC polarization measurements revealed a significant increase of the electronic conductivities with higher CP content. Integration in sulfide half-cells showed promising results in the improved initial discharge capacities, signifying that the addition of the CP allowed to address CAM more

efficiently in the cathode composite. These results serve as the foundation of further studies in the development of more efficient, scalable, and greener routes to the preparation of cathode composites for applications in ASSBs.

Supporting Information

Chemical structure of PEDOT:PSS, additional SEM and EDX images for as-prepared and pressed powders, TGA and DSC traces for additional samples, schematic for the preparation of the Li_3InCl_6|CP composites, additional PXRD results for composites prepared under unoptimized conditions, DC polarization data, additional charge-discharge curves, and Coulombic efficiencies for all cells.

Acknowledgements

This work was funded by the Ministry of Culture and Science of the State North Rhine-Westphalia as part of the International Graduate School BACCARA. We are grateful to Münster Electrochemical Energy Technology (MEET), the Center for Nanotechnology (CeNTech) and the Zeier Research Group at the University of Münster for access to lab facilities. Dr. Michael R. Nellist is acknowledged for support at initial stages of this project. Special thanks are offered to Debbie Berghus who performed the DSC and TGA measurements. N.M.V-B. gratefully acknowledges the support of the Helmholtz Association *via* the Young Investigator Group Program.

References

(1) Masias, A.; Marcicki, J.; Paxton, W. A. Opportunities and Challenges of Lithium Ion Batteries in Automotive Applications. *ACS Energy Lett* **2021**, *6* (2), 621–630. https://doi.org/10.1021/acsenergylett.0c02584.

(2) Bates, A. M.; Preger, Y.; Torres-Castro, L.; Harrison, K. L.; Harris, S. J.; Hewson, J. Are Solid-State Batteries Safer than Lithium-Ion Batteries? *Joule* **2022**, *6* (4), 742–755. https://doi.org/10.1016/j.joule.2022.02.007.

(3) Janek, J.; Zeier, W. G. A Solid Future for Battery Development. *Nat Energy* **2016**, *1* (9), 16141. https://doi.org/10.1038/nenergy.2016.141.

(4) Famprikis, T.; Canepa, P.; Dawson, J. A.; Islam, M. S.; Masquelier, C. Fundamentals of Inorganic Solid-State Electrolytes for Batteries. *Nat Mater* **2019**, *18* (12), 1278–1291. https://doi.org/10.1038/s41563-019-0431-3.

(5) Krauskopf, T.; Richter, F. H.; Zeier, W. G.; Janek, J. Physicochemical Concepts of the Lithium Metal Anode in Solid-State Batteries. *Chem Rev* **2020**, *120* (15), 7745–7794. https://doi.org/10.1021/acs.chemrev.0c00431.

(6) Cheng, X. B.; Zhao, C. Z.; Yao, Y. X.; Liu, H.; Zhang, Q. Recent Advances in Energy Chemistry between Solid-State Electrolyte and Safe Lithium-Metal Anodes. *Chem* **2019**, *5* (1), 74–96. https://doi.org/10.1016/j.chempr.2018.12.002.
(7) Kim, K. J.; Balaish, M.; Wadaguchi, M.; Kong, L.; Rupp, J. L. M. Solid-State Li–Metal Batteries: Challenges and Horizons of Oxide and Sulfide Solid Electrolytes and Their Interfaces. *Adv Energy Mater* **2021**, *11* (1), 2002689. https://doi.org/10.1002/aenm.202002689.
(8) Shi, T.; Zhang, Y. Q.; Tu, Q.; Wang, Y.; Scott, M. C.; Ceder, G. Characterization of Mechanical Degradation in an All-Solid-State Battery Cathode. *J Mater Chem A Mater* **2020**, *8* (34), 17399–17404. https://doi.org/10.1039/d0ta06985j.
(9) Minnmann, P.; Strauss, F.; Bielefeld, A.; Ruess, R.; Adelhelm, P.; Burkhardt, S.; Dreyer, S. L.; Trevisanello, E.; Ehrenberg, H.; Brezesinski, T.; Richter, F. H.; Janek, J. Designing Cathodes and Cathode Active Materials for Solid-State Batteries. *Adv Energy Mater* **2022**, *12* (35), 2201425. https://doi.org/10.1002/aenm.202201425.
(10) Zhang, J.; Chen, Z.; Ai, Q.; Terlier, T.; Hao, F.; Liang, Y.; Guo, H.; Lou, J.; Yao, Y. Microstructure Engineering of Solid-State Composite Cathode via Solvent-Assisted Processing. *Joule* **2021**, *5* (7), 1845–1859. https://doi.org/10.1016/j.joule.2021.05.017.
(11) Sen, S.; Trevisanello, E.; Niemöller, E.; Shi, B. X.; Simon, F. J.; Richter, F. H. The Role of Polymers in Lithium Solid-State Batteries with Inorganic Solid Electrolytes. *J Mater Chem A Mater* **2021**, *9* (35), 18701–18732. https://doi.org/10.1039/d1ta02796d.
(12) Wang, M. J.; Kazyak, E.; Dasgupta, N. P.; Sakamoto, J. Transitioning Solid-State Batteries from Lab to Market: Linking Electro-Chemo-Mechanics with Practical Considerations. *Joule* **2021**, *5* (6), 1371–1390. https://doi.org/10.1016/j.joule.2021.04.001.
(13) Fan, L. Z.; He, H.; Nan, C. W. Tailoring Inorganic–Polymer Composites for the Mass Production of Solid-State Batteries. *Nat Rev Mater* **2021**, *6* (11), 1003–1019. https://doi.org/10.1038/s41578-021-00320-0.
(14) Wang, K.; Ye, Q.; Zhang, J.; Huang, H.; Gan, Y.; He, X.; Zhang, W. Halide Electrolyte Li_3InCl_6-Based All-Solid-State Lithium Batteries With Slurry-Coated $LiNi_{0.8}Co_{0.1}Mn_{0.1}O_2$ Composite Cathode: Effect of Binders. *Front Mater* **2021**, *8*, 727617. https://doi.org/10.3389/fmats.2021.727617.
(15) Ensafi, A. A.; Mousaabadi, K. Z.; Fazel-Zarandi, R. Application of Conductive Polymers in Electrochemistry. In *ACS Symposium Series*; American Chemical Society, 2022; Vol. 1405, pp 185–217. https://doi.org/10.1021/bk-2022-1405.ch008.
(16) Sengodu, P.; Deshmukh, A. D. Conducting Polymers and Their Inorganic Composites for Advanced Li-Ion Batteries: A Review. *RSC Adv* **2015**, *5* (52), 42109–42130. https://doi.org/10.1039/c4ra17254j.
(17) Das, P. R.; Komsiyska, L.; Osters, O.; Wittstock, G. PEDOT: PSS as a Functional Binder for Cathodes in Lithium Ion Batteries. *J Electrochem Soc* **2015**, *162* (4), A674–A678. https://doi.org/10.1149/2.0581504jes.
(18) Das, P.; Elizalde-Segovia, R.; Zayat, B.; Salamat, C. Z.; Pace, G.; Zhai, K.; Vincent, R. C.; Dunn, B. S.; Segalman, R. A.; Tolbert, S. H.; Narayan, S. R.; Thompson, B. C. Enhancing the Ionic Conductivity of Poly(3,4-Propylenedioxythiophenes) with Oligoether Side Chains for Use as Conductive Cathode Binders in Lithium-Ion Batteries. *Chemistry of Materials* **2022**, *34* (6), 2672–2686. https://doi.org/10.1021/acs.chemmater.1c03971.
(19) Zhao, Y. M.; Yue, F. S.; Li, S. C.; Zhang, Y.; Tian, Z. R.; Xu, Q.; Xin, S.; Guo, Y. G. Advances of Polymer Binders for Silicon-Based Anodes in High Energy Density Lithium-Ion Batteries. *InfoMat* **2021**, *3* (5), 460–501. https://doi.org/10.1002/inf2.12185.

(20) Zeng, W.; Wang, L.; Peng, X.; Liu, T.; Jiang, Y.; Qin, F.; Hu, L.; Chu, P. K.; Huo, K.; Zhou, Y. Enhanced Ion Conductivity in Conducting Polymer Binder for High-Performance Silicon Anodes in Advanced Lithium-Ion Batteries. *Adv Energy Mater* **2018**, *8* (11), 1702314. https://doi.org/10.1002/aenm.201702314.
(21) Deng, S.; Jiang, M.; Chen, N.; Li, W.; Zheng, M.; Chen, W.; Li, R.; Huang, H.; Wang, J.; Singh, C. V.; Sun, X. Regulating Electronic Conductivity at Cathode Interface for Low-Temperature Halide-Based All-Solid-State Batteries. *Adv Funct Mater* **2022**, *32* (45), 2205594. https://doi.org/10.1002/adfm.202205594.
(22) Zhu, Y.; He, X.; Mo, Y. Origin of Outstanding Stability in the Lithium Solid Electrolyte Materials: Insights from Thermodynamic Analyses Based on First-Principles Calculations. *ACS Appl Mater Interfaces* **2015**, *7* (42), 23685–23693. https://doi.org/10.1021/acsami.5b07517.
(23) Kato, Y.; Hori, S.; Saito, T.; Suzuki, K.; Hirayama, M.; Mitsui, A.; Yonemura, M.; Iba, H.; Kanno, R. High-Power All-Solid-State Batteries Using Sulfide Superionic Conductors. *Nat Energy* **2016**, *1* (4), 16030. https://doi.org/10.1038/nenergy.2016.30.
(24) Brahmbhatt, T.; Yang, G.; Self, E.; Nanda, J. Cathode–Sulfide Solid Electrolyte Interfacial Instability: Challenges and Solutions. *Front Energy Res* **2020**, *8*, 570754. https://doi.org/10.3389/fenrg.2020.570754.
(25) Wei, R.; Chen, S.; Gao, T.; Liu, W. Challenges, Fabrications and Horizons of Oxide Solid Electrolytes for Solid-state Lithium Batteries. *Nano Select* **2021**, *2* (12), 2256–2274. https://doi.org/10.1002/nano.202100110.
(26) Kwak, H.; Wang, S.; Park, J.; Liu, Y.; Kim, K. T.; Choi, Y.; Mo, Y.; Jung, Y. S. Emerging Halide Superionic Conductors for All-Solid-State Batteries: Design, Synthesis, and Practical Applications. *ACS Energy Lett* **2022**, *7* (5), 1776–1805. https://doi.org/10.1021/acsenergylett.2c00438.
(27) Park, D.; Park, H.; Lee, Y.; Kim, S. O.; Jung, H. G.; Chung, K. Y.; Shim, J. H.; Yu, S. Theoretical Design of Lithium Chloride Superionic Conductors for All-Solid-State High-Voltage Lithium-Ion Batteries. *ACS Appl Mater Interfaces* **2020**, *12* (31), 34806–34814. https://doi.org/10.1021/acsami.0c07003.
(28) Li, X.; Liang, J.; Luo, J.; Norouzi Banis, M.; Wang, C.; Li, W.; Deng, S.; Yu, C.; Zhao, F.; Hu, Y.; Sham, T. K.; Zhang, L.; Zhao, S.; Lu, S.; Huang, H.; Li, R.; Adair, K. R.; Sun, X. Air-Stable Li3InCl6 Electrolyte with High Voltage Compatibility for All-Solid-State Batteries. *Energy Environ Sci* **2019**, *12* (9), 2665–2671. https://doi.org/10.1039/c9ee02311a.
(29) Li, X.; Liang, J.; Chen, N.; Luo, J.; Adair, K. R.; Wang, C.; Banis, M. N.; Sham, T.; Zhang, L.; Zhao, S.; Lu, S.; Huang, H.; Li, R.; Sun, X. Water-Mediated Synthesis of a Superionic Halide Solid Electrolyte. *Angewandte Chemie* **2019**, *58* (46), 16427–16432. https://doi.org/10.1002/ange.201909805.
(30) Wang, C.; Liang, J.; Jiang, M.; Li, X.; Mukherjee, S.; Adair, K.; Zheng, M.; Zhao, Y.; Zhao, F.; Zhang, S.; Li, R.; Huang, H.; Zhao, S.; Zhang, L.; Lu, S.; Singh, C. V.; Sun, X. Interface-Assisted in-Situ Growth of Halide Electrolytes Eliminating Interfacial Challenges of All-Inorganic Solid-State Batteries. *Nano Energy* **2020**, *76*, 105015. https://doi.org/10.1016/j.nanoen.2020.105015.
(31) Culver, S. P.; Koerver, R.; Zeier, W. G.; Janek, J. On the Functionality of Coatings for Cathode Active Materials in Thiophosphate-Based All-Solid-State Batteries. *Adv Energy Mater* **2019**, *9* (24), 1900626. https://doi.org/10.1002/aenm.201900626.
(32) Sacci, R. L.; Bennett, T. H.; Drews, A. R.; Anandan, V.; Kirkham, M. J.; Daemen, L. L.; Nanda, J. Phase Evolution during Lithium-Indium Halide Superionic Conductor Dehydration. *J Mater Chem A Mater* **2021**, *9* (2), 990–996. https://doi.org/10.1039/d0ta10012a.

(33) Liu, H. W.; Lin, C. C.; Chang, P. Y.; Haw, S. C.; Sheu, H. S.; Chen, J. M.; Chen, C. C.; Jeng, R. J.; Wu, N. L. Reducing Oxy-Contaminations for Enhanced Li-Ion Conductivity of Halide-Based Solid Electrolyte in Water-Mediated Synthesis. *Journal of Solid State Electrochemistry* **2022**, *26* (9), 2089–2096. https://doi.org/10.1007/s10008-022-05213-y.
(34) Örnek, C.; Leygraf, C.; Pan, J. On the Volta Potential Measured by SKPFM–Fundamental and Practical Aspects with Relevance to Corrosion Science. *Corrosion Engineering Science and Technology* **2019**, *54* (3), 185–198. https://doi.org/10.1080/1478422X.2019.1583436.
(35) Zhang, W.; Weber, D. A.; Weigand, H.; Arlt, T.; Manke, I.; Schröder, D.; Koerver, R.; Leichtweiss, T.; Hartmann, P.; Zeier, W. G.; Janek, J. Interfacial Processes and Influence of Composite Cathode Microstructure Controlling the Performance of All-Solid-State Lithium Batteries. *ACS Appl Mater Interfaces* **2017**, *9*, 17835–17845. https://doi.org/10.1021/acsami.7b01137.
(36) Santhosha, A. L.; Medenbach, L.; Buchheim, J. R.; Adelhelm, P. The Indium−Lithium Electrode in Solid-State Lithium-Ion Batteries: Phase Formation, Redox Potentials, and Interface Stability. *Batter Supercaps* **2019**, *2* (6), 524–529. https://doi.org/10.1002/batt.201800149.
(37) Kochetkov, I.; Zuo, T. T.; Ruess, R.; Singh, B.; Zhou, L.; Kaup, K.; Janek, J.; Nazar, L. Different Interfacial Reactivity of Lithium Metal Chloride Electrolytes with High Voltage Cathodes Determines Solid-State Battery Performance. *Energy Environ Sci* **2022**, *15* (9), 3933–3944. https://doi.org/10.1039/d2ee00803c.
(38) Wang, K.; Ren, Q.; Gu, Z.; Duan, C.; Wang, J.; Zhu, F.; Fu, Y.; Hao, J.; Zhu, J.; He, L.; Wang, C. W.; Lu, Y.; Ma, J.; Ma, C. A Cost-Effective and Humidity-Tolerant Chloride Solid Electrolyte for Lithium Batteries. *Nat Commun* **2021**, *12*, 4410. https://doi.org/10.1038/s41467-021-24697-2.
(39) Li, X.; Liang, J.; Yang, X.; Adair, K. R.; Wang, C.; Zhao, F.; Sun, X. Progress and Perspectives on Halide Lithium Conductors for All-Solid-State Lithium Batteries. *Energy Environ Sci* **2020**, *13* (5), 1429–1461. https://doi.org/10.1039/c9ee03828k.
(40) Wang, S.; Xu, X.; Cui, C.; Zeng, C.; Liang, J.; Fu, J.; Zhang, R.; Zhai, T.; Li, H. Air Sensitivity and Degradation Evolution of Halide Solid State Electrolytes upon Exposure. *Adv Funct Mater* **2022**, *32* (7), 2108805. https://doi.org/10.1002/adfm.202108805.
(41) Li, W.; Liang, J.; Li, M.; Adair, K. R.; Li, X.; Hu, Y.; Xiao, Q.; Feng, R.; Li, R.; Zhang, L.; Lu, S.; Huang, H.; Zhao, S.; Sham, T. K.; Sun, X. Unraveling the Origin of Moisture Stability of Halide Solid-State Electrolytes by in Situ and Operando Synchrotron X-Ray Analytical Techniques. *Chemistry of Materials* **2020**, *32* (16), 7019–7027. https://doi.org/10.1021/acs.chemmater.0c02419.
(42) Shi, W.; Yao, Q.; Qu, S.; Chen, H.; Zhang, T.; Chen, L. Micron-Thick Highly Conductive Pedot Films Synthesized via Self-Inhibited Polymerization: Roles of Anions. *NPG Asia Mater* **2017**, *9*, e405. https://doi.org/10.1038/am.2017.107.
(43) Chiu, W. W.; Travaš-Sejdić, J.; Cooney, R. P.; Bowmaker, G. A. Studies of Dopant Effects in Poly(3,4-Ethylenedioxythiophene) Using Raman Spectroscopy. *Journal of Raman Spectroscopy* **2006**, *37* (12), 1354–1361. https://doi.org/10.1002/jrs.1545.
(44) Chang, S. H.; Chiang, C. H.; Kao, F. S.; Tien, C. L.; Wu, C. G. Unraveling the Enhanced Electrical Conductivity of PEDOT:PSS Thin Films for ITO-Free Organic Photovoltaics. *IEEE Photonics J* **2014**, *6* (4), 8400307. https://doi.org/10.1109/JPHOT.2014.2331254.
(45) Antiohos, D.; Folkes, G.; Sherrell, P.; Ashraf, S.; Wallace, G. G.; Aitchison, P.; Harris, A. T.; Chen, J.; Minett, A. I. Compositional Effects of PEDOT-PSS/Single Walled

Carbon Nanotube Films on Supercapacitor Device Performance. *J Mater Chem* **2011**, *21* (40), 15987–15994. https://doi.org/10.1039/c1jm12986d.
(46) Han, Y.-K.; Chang, M.-Y.; Huang, W.-Y.; Pan, H.-Y.; Ho, K.-S.; Hsieh, T.-H.; Pan, S.-Y. Improved Performance of Polymer Solar Cells Featuring One-Dimensional PEDOT Nanorods in a Modified Buffer Layer. *J Electrochem Soc* **2011**, *158* (3), K88–K93. https://doi.org/10.1149/1.3534201.
(47) Chen, R.; Sun, K.; Zhang, Q.; Zhou, Y.; Li, M.; Sun, Y.; Wu, Z.; Wu, Y.; Li, X.; Xi, J.; Ma, C.; Zhang, Y.; Ouyang, J. Sequential Solution Polymerization of Poly(3,4-Ethylenedioxythiophene)Using V_2O_5 as Oxidant for Flexible Touch Sensors. *iScience* **2019**, *12*, 66–75. https://doi.org/10.1016/j.isci.2019.01.003.
(48) Helm, B.; Schlem, R.; Wankmiller, B.; Banik, A.; Gautam, A.; Ruhl, J.; Li, C.; Hansen, M. R.; Zeier, W. G. Exploring Aliovalent Substitutions in the Lithium Halide Superionic Conductor $Li_{3-x}In_{1-x}Zr_xCl_6$ ($0 \leq x \leq 0.5$). *Chemistry of Materials* **2021**, *33* (12), 4773–4782. https://doi.org/10.1021/acs.chemmater.1c01348.
(49) Salerno, M.; Dante, S. Scanning Kelvin Probe Microscopy: Challenges and Perspectives towards Increased Application on Biomaterials and Biological Samples. *Materials* **2018**, *11* (6), 951. https://doi.org/10.3390/ma11060951.
(50) Melitz, W.; Shen, J.; Kummel, A. C.; Lee, S. Kelvin Probe Force Microscopy and Its Application. *Surf Sci Rep* **2011**, *66* (1), 1–27. https://doi.org/10.1016/j.surfrep.2010.10.001.
(51) Zhu, Y.; Wu, S.; Pan, Y.; Zhang, X.; Yan, Z.; Xiang, Y. Reduced Energy Barrier for Li+ Transport Across Grain Boundaries with Amorphous Domains in LLZO Thin Films. *Nanoscale Res Lett* **2020**, *15*, 153. https://doi.org/10.1186/s11671-020-03378-x.
(52) Riegger, L. M.; Schlem, R.; Sann, J.; Zeier, W. G.; Janek, J. Lithium-Metal Anode Instability of the Superionic Halide Solid Electrolytes and the Implications for Solid-State Batteries. *Angewandte Chemie International Edition* **2021**, *60* (12), 6718–6723. https://doi.org/10.1002/anie.202015238.
(53) Wang, C.; Liang, J.; Kim, J. T.; Sun, X. Prospects of Halide-Based All-Solid-State Batteries: From Material Design to Practical Application. *Sci Adv* **2022**, *8* (36), eadc9516.
(54) Minnmann, P.; Quillman, L.; Burkhardt, S.; Richter, F. H.; Janek, J. Editors' Choice—Quantifying the Impact of Charge Transport Bottlenecks in Composite Cathodes of All-Solid-State Batteries. *J Electrochem Soc* **2021**, *168* (4), 040537. https://doi.org/10.1149/1945-7111/abf8d7.
(55) Hendriks, T.; Lange, M.; Kiens, E.; Baeumer, C.; Zeier, W. Balancing Partial Ionic and Electronic Transport for Optimized Cathode Utilization of High-voltage LiMn2O4 / Li3InCl6 Solid-state Batteries. *Batter Supercaps* **2023**. https://doi.org/10.1002/batt.202200544.
(56) Ohno, S.; Koerver, R.; Dewald, G.; Rosenbach, C.; Titscher, P.; Steckermeier, D.; Kwade, A.; Janek, J.; Zeier, W. G. Observation of Chemomechanical Failure and the Influence of Cutoff Potentials in All-Solid-State Li-S Batteries. *Chemistry of Materials* **2019**, *31* (8), 2930–2940. https://doi.org/10.1021/acs.chemmater.9b00282.

TOC:

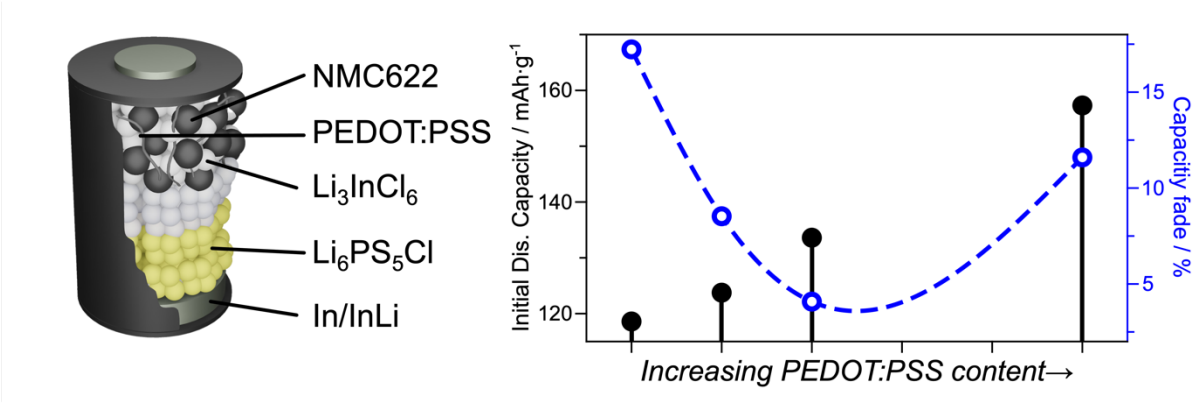
NMC622
PEDOT:PSS
Li_3InCl_6
Li_6PS_5Cl
In/InLi
Initial Dis. Capacity / mAh·g^{-1}
160
140
120
15
10
5
Capacitiy fade / %
Increasing PEDOT:PSS content→